*Journal of The Electrochemical Society*, **155** (10) B1023-B1028 (2008)
0013-4651/2008/155(10)/B1023/6/$23.00 © The Electrochemical Society



# Characterization of $GdBa_{1-x}Sr_xCo_2O_{5+\delta}$ ($0 \leqslant x \leqslant 1.0$) Double Perovskites as Cathodes for Solid Oxide Fuel Cells

**J.-H. Kim,[a] F. Prado,[a,b] and A. Manthiram[a,*,z]**

[a]*Electrochemical Energy Laboratory & Materials Science and Engineering Program, University of Texas at Austin, Austin, Texas 78712, USA*
[b]*Departamento de Física, Universidad Nacional del Sur, 8000 Bahía Blanca, Argentina*

The effect of $Sr^{2+}$ substitution for $Ba^{2+}$ on the crystal chemistry, oxygen content, thermal expansion, electrical conductivity, and catalytic activity for oxygen reduction reaction (ORR) of the double perovskite oxides $GdBa_{1-x}Sr_xCo_2O_{5+\delta}$ has been investigated for $0 \leqslant x \leqslant 1.0$. The $GdBa_{1-x}Sr_xCo_2O_{5+\delta}$ system exhibits a structural change from orthorhombic ($x = 0$) to tetragonal ($0.2 \leqslant x \leqslant 0.6$) to orthorhombic ($x = 1$) with increasing Sr content. The difference in ionic radii between $(Ba_{1-x}Sr_x)^{2+}$ and $Gd^{3+}$ plays a dominant role in determining the oxygen-content value in $GdBa_{1-x}Sr_xCo_2O_{5+\delta}$, and the oxygen content and the oxidation state of cobalt increase with increasing Sr content. The electrical conductivity of the $GdBa_{1-x}Sr_xCo_2O_{5+\delta}$ system increases with Sr content due to an increasing oxygen content and a straightening of the O–Co–O bonds as evidenced by the structural change from orthorhombic to tetragonal. Sr substitution also improves the chemical stability of the $GdBa_{1-x}Sr_xCo_2O_{5+\delta}$ cathodes in contact with the $Ce_{0.9}Gd_{0.1}O_{1.95}$ and $La_{0.8}Sr_{0.2}Ga_{0.8}Mg_{0.2}O_{2.8}$ electrolytes at 1100°C. The $x = 0.2$ and 0.6 samples with a tetragonal structure exhibit higher catalytic activity for ORR in single-cell solid oxide fuel cell than the $x = 0$ and 1.0 samples with an orthorhombic structure.
 [DOI: 10.1149/1.2965792] 

Manuscript submitted May 15, 2008; revised manuscript received July 7, 2008. Published August 8, 2008.

Several groups have been focusing extensively in recent years on the crystal chemistry and low-temperature electrical and magnetic properties of $LnBaCo_2O_{5+\delta}$ (Ln = Pr, Nd, Sm, Eu, Gd, Tb, Dy, Ho, and Y) oxides.[1-8] These oxides have perovskite-related structures in which the LnO and BaO layers alternate along the *c* axis. They adopt tetragonal or orthorhombic symmetry depending on the $Ln^{3+}$ ions and the oxygen content $5 + \delta$ value,[4-9] which varies widely with the $Ln^{3+}$ ion and synthesis conditions. For example, the oxygen content decreases with decreasing size of $Ln^{3+}$ ions or with decreasing oxygen partial pressure during synthesis.[4-10] Structural analysis has shown that the oxygen vacancies are located exclusively in the $Ln^{3+}$ layers due to the smaller size of the $Ln^{3+}$ ions compared to $Ba^{2+}$, which results in the formation of $CoO_5$ square pyramids and $CoO_6$ octahedra.[3,5]

Recently, the mixed ionic–electronic conducting properties of these $LnBaCo_2O_{5+\delta}$ (Ln = Pr, Nd, Sm, Gd, and Y) double perovskites at high temperatures have begun to be investigated.[10-13] The $LnBaCo_2O_{5+\delta}$ oxides show a metal-to-insulator (M-I) transition with decreasing temperature below $T_{MI} \approx 360$ K for Ln = Sm, Eu, and Gd.[1,2,4,5,7] A few groups have also reported fast oxide ion conduction in the $LnBaCo_2O_{5+\delta}$ oxides.[11-13] Especially, the oxide ion diffusion and surface exchange kinetics have been measured using $^{18}O/^{16}O$ isotope exchange depth profile in the Ln = Pr and Gd systems and have been compared with those of other perovskite oxides such as $La_{0.5}Sr_{0.5}CoO_{3-\delta}$, $La_{0.6}Sr_{0.4}Co_{0.2}Fe_{0.8}O_{3-\delta}$, and $La_{0.8}Sr_{0.2}MnO_{3-\delta}$.[12,13] These studies have suggested the potential of these double perovskites as cathode materials for solid oxide fuel cells (SOFCs).

Our group recently characterized the $LnBaCo_2O_{5+\delta}$ oxides with Ln = La, Nd, Sm, Gd, and Y as cathodes for SOFCs.[10] Our results showed that both the thermal expansion coefficient (TEC) and the catalytic activity for the oxygen reduction reaction (ORR) decrease with decreasing size of the $Ln^{3+}$ ions from Ln = La to Gd. In addition, $GdBaCo_2O_{5+\delta}$ was found to be chemically unstable in contact with the $La_{0.8}Sr_{0.2}Ga_{0.8}Mg_{0.2}O_{2.8}$ (LSGM) and $Ce_{0.9}Gd_{0.1}O_{1.95}$ (GDC) electrolytes at 1100°C. With an aim to improve the catalytic activity for ORR and the chemical stability against LSGM and GDC electrolyte materials, we present here an investigation of the $GdBa_{1-x}Sr_xCo_2O_{5+\delta}$ system for $0 \leqslant x \leqslant 1.0$. The variations in crystal chemistry, oxygen content, chemical stability in contact with the electrolyte, and catalytic activity for ORR with Sr content are presented.

## Experimental

The $GdBa_{1-x}Sr_xCo_2O_{5+\delta}$ ($0 \leqslant x \leqslant 1.0$) oxides were synthesized by conventional solid-state-reaction methods. Required amounts of $Gd_2O_3$, $BaCO_3$, $SrCO_3$, and $Co_3O_4$ were thoroughly mixed with ballmilling in ethanol for 24 h and calcined at 1000°C for 12 h in air. The calcined powders were then ground, pressed into pellets, and sintered at 1200°C for 24 h in air. The resulting products were ground and finally heated at 900°C for 6 h in air, followed by slow cooling to room temperature at a rate of 1°C/min to maximize the oxygen content. The LSGM electrolyte disks were prepared by firing required amounts of $La_2O_3$, $SrCO_3$, $Ga_2O_3$, and MgO at 1100°C for 5 h, followed by pelletizing and sintering at 1500°C for 10 h. GDC and $La_{0.4}Ce_{0.6}O_{1.8}$ (LDC) powders were synthesized by the glycine-nitrate combustion method.[14,15] For the anode, NiO and GDC (Ni:GDC = 70:30 vol %) were ballmilled in ethanol for 48 h.

The products thus obtained were characterized by X-ray diffraction (XRD), and the XRD data were fitted with the Rietveld method using the Fullprof program.[16] The average oxidation state of cobalt and the room-temperature oxygen content values were determined by iodometric titration.[17] Thermogravimetric analysis (TGA) and thermal expansion data were collected with a Perkin-Elmer Series 7 thermal analysis system. The TGA experiments were carried out from room temperature to 950°C with a heating/cooling rate of 3°C/min. The TECs of the sintered samples were measured in the temperature range of 80–900°C with a heating/cooling rate of 5°C/min, with an intermediate dwelling at 900°C for 0.5 h. The heating/cooling cycles were repeated three times and their average TECs were determined. Electrical conductivity of the pellets was measured with a four-probe dc method using a Van der Pauw configuration in the temperature range of 40–900°C.[18,19] The specimens for the reactivity tests were obtained by mixing the $GdBa_{1-x}Sr_xCo_2O_{5+\delta}$ oxides and the electrolyte powders in a 1:1 weight ratio, followed by calcining in air at 1100°C for 0.5 and 1 h, respectively, for LSGM and GDC.

Electrochemical performances of the $GdBa_{1-x}Sr_xCo_2O_{5+\delta}$ cathodes were evaluated with an electrolyte-supported single-cell SOFC. All the electrode materials were mixed with an organic binder (Heraeus V006) to form slurries and then applied onto the surface of a dense LSGM pellet (500 μm thickness) by screen printing. To prevent the formation of $LaNiO_3$ or $La_2NiO_4$ at the anode/electrolyte

* Electrochemical Society Active Member.
z E-mail: rmanth@mail.utexas.edu

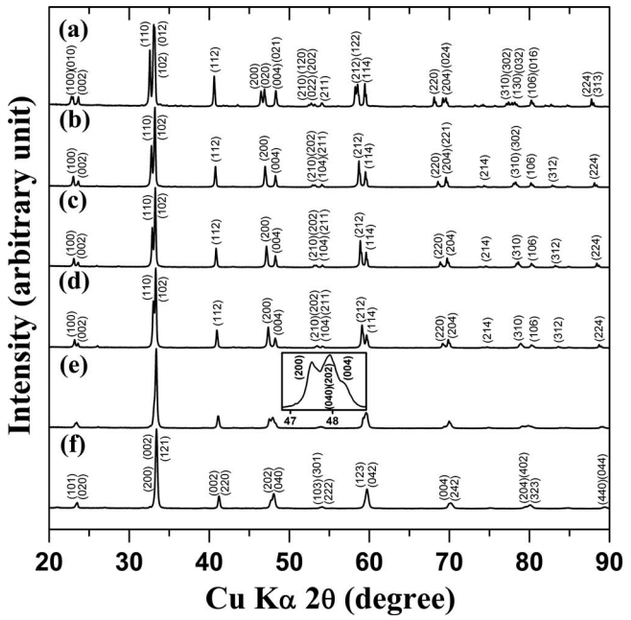


**Figure 1.** XRD patterns of the $GdBa_{1-x}Sr_xCo_2O_{5+\delta}$ samples: (a) $x = 0$, (b) $x = 0.2$, (c) $x = 0.4$, (d) $x = 0.6$, (e) $x = 0.8$, and (f) $x = 1.0$.

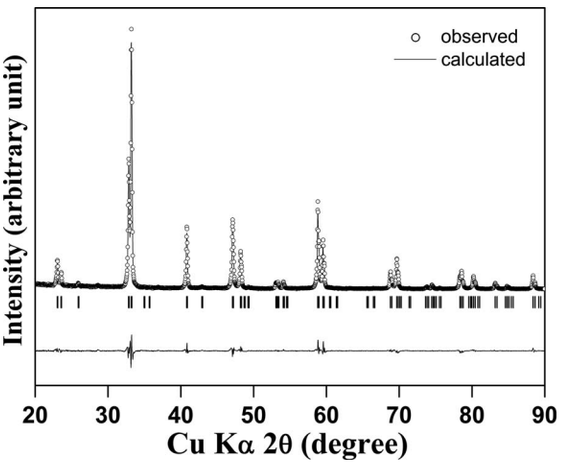


**Figure 2.** XRD pattern, calculated profile, peak position, and the difference between observed and calculated profiles for the $GdBa_{0.6}Sr_{0.4}Co_2O_{5+\delta}$ sample.

interface, an LDC buffer layer was first prepared by screen printing onto the anode side of the LSGM electrolyte.[20] After heating the buffer layer at 1000°C for 1 h, the NiO–GDC cermet anode was screen printed onto the LDC layer and heated at 1300°C for 0.5 h. Similarly, a composite layer consisting of $GdBa_{1-x}Sr_xCo_2O_{5+\delta}$ and LSGM (1:1 wt ratio) was first prepared by screen printing onto the cathode side of the LSGM electrolyte and heated at 1100°C for 0.5 h. The $GdBa_{1-x}Sr_xCo_2O_{5+\delta}$ cathode layer was subsequently screen printed onto the $GdBa_{1-x}Sr_xCo_2O_{5+\delta}$–LSGM composite layer and heated at 1000°C for 3 h. The intermediate $GdBa_{1-x}Sr_xCo_2O_{5+\delta}$–LSGM composite layer ensures good interfacial contact between the LSGM electrolyte and the $LnBaCo_2O_{5+\delta}$ cathode. The microstructures of the LSGM-cathode interfaces were observed with a scanning electron microscope (SEM, JEOL JSM-5610). Each electrode had a circular shape with a diameter of 1 cm, and its effective electrode area was 0.79 $cm^2$. Pt mesh with an area of 0.25 $cm^2$ was attached to the electrodes with Pt wire and Pt paste as a current collector. During the single-cell performance test, humidified $H_2$ (~3% $H_2O$ at 25°C) and air were supplied as fuel and oxidant, respectively, at a rate of 100 $cm^3$/min.

## Results and Discussion

Figure 1 shows the XRD patterns of the $GdBa_{1-x}Sr_xCo_2O_{5+\delta}$ ($0 \leq x \leq 1.0$) samples. All the reflections of the parent $GdBaCo_2O_{5+\delta}$ sample could be indexed with an orthorhombic structure with the space group of *Pmmm*.[1,5,13] Iodometric titration indicates the room-temperature oxygen content to be 5.61 (Table I) in $GdBaCo_2O_{5+\delta}$. The fully Sr-substituted $GdSrCo_2O_{5+\delta}$ has been reported to have an orthorhombic structure with the space group of *Pnma*.[21,22] The XRD pattern in Fig. 1f is consistent with this earlier result, and our chemical analysis indicates an oxygen content of 6.0 as seen in Table I. The room-temperature crystal structures of the intermediate compositions with $0.2 \leq x \leq 0.6$ in $GdBa_{1-x}Sr_xCo_2O_{5+\delta}$ could be refined on the basis of a tetragonal symmetry with the space group *P4/mmm*. As an example, the experimental XRD data, calculated profile, and the difference between the experimental and calculated profiles are shown in Fig. 2 for the $x = 0.4$ sample. There is good agreement between the experimental and calculated profiles, and the resulting atomic positions and the quality of refinement are given in Table II. The refinement was also performed assuming that Sr is partly located at the Gd site. However, the Sr amount at the Gd site reduced to zero at the end of refinement, suggesting that Sr prefers the Ba site. This is consistent with an earlier report by Nakamura et al.[23] that Sr occupies the Ba sites in the $(Ba_{1-x}Sr_x)SmFe_2O_5$ double perovskite. The $x = 0.8$ sample in Fig. 1e consists of a mixture of tetragonal (*P4/mmm*) and orthorhombic (*Pnma*) phases as revealed by the inset at $2\theta \approx 48°$. The unit cell volume given in Table I decreases with increasing Sr content due to substitution of a smaller $Sr^{2+}$ for $Ba^{2+}$ and oxidation of the larger $Co^{3+}$ ions into the smaller $Co^{4+}$ ions, as indicated by an increase in the oxygen content value (Table I).

Iodometric titration data in Table I indicate that the room-temperature oxygen content and the oxidation state of cobalt increase with increasing Sr content $x$. Although one would generally anticipate the more electropositive $Ba^{2+}$ ions to enhance the stabili-

**Table I. Structural parameters, chemical analysis data, and TEC of the $GdBa_{1-x}Sr_xCo_2O_{5+\delta}$ oxides.**

| $x$ | Space group | $Z$ | $a$ (Å) | $b$ (Å) | $c$ (Å) | V (Å$^3$) | Oxidation state of Co | Oxygen content ($5+\delta$) | TEC × $10^6$(°C$^{-1}$) | | |
|---|---|---|---|---|---|---|---|---|---|---|---|
| | | | | | | | | | 80–900°C | 80–300°C | 300–900°C |
| 0.0 | *Pmmm* | 1 | 3.876 | 3.912 | 7.541 | 114.367 | 3.11 | 5.61 | 16.6 | 16.3 | 17.7 |
| 0.2 | *P4/mmm* | 1 | 3.872 | 3.872 | 7.550 | 113.155 | 3.19 | 5.69 | 18.0 | 15.9 | 18.7 |
| 0.4 | *P4/mmm* | 1 | 3.856 | 3.856 | 7.546 | 112.194 | 3.29 | 5.79 | 18.3 | 16.0 | 19.8 |
| 0.6 | *P4/mmm* | 1 | 3.840 | 3.840 | 7.549 | 111.304 | 3.33 | 5.83 | 19.5 | 15.7 | 20.9 |
| 1.0[a] | *Pnma* | 4 | 5.373 | 7.572 | 5.402 | 219.763 | 3.50 | 6.00 | 18.8 | 15.3 | 19.9 |

[a] Lattice parameter and volume are based on the chemical formula $Gd_{0.5}Sr_{0.5}CoO_3$.

**Table II. Room-temperature atomic positions in $GdBa_{1-x}Sr_xCo_2O_{5+\delta}$.[a]**

| $x$ | $z_{Co}$ | $z_{O(2)}$ | $R_{wp}$ | $\chi^2$ |
|---|---|---|---|---|
| 0.2 | 0.2566 | 0.2832 | 13.5 | 3.21 |
| 0.4 | 0.2523 | 0.2788 | 11.5 | 2.93 |
| 0.6 | 0.2520 | 0.2754 | 10.9 | 3.24 |

[a] Atomic positions are Gd (0,0,1/2), Ba/Sr (0,0,0), Co (1/2,1/2,z), O(1) (1/2,1/2,0), O(2) (1/2,0,z), and O(3) (1/2,1/2,1/2).

zation of the higher valent $Co^{4+}$ ions, the ordering between $Ba^{2+}$ and $Gd^{3+}$ ions in alternate layers due to a larger size difference between them and the tendency of the smaller $Gd^{3+}$ ions to adopt a coordination number less than 12 result in a lower oxygen-content value for $GdBaCo_2O_{5+\delta}$. A smaller size difference between the $Sr^{2+}$ and $Gd^{3+}$ ions and a consequent perturbation of the ordering between the two layers (Ba and Gd) result in a tendency to increase the coordination number and consequently the oxygen-content values. A similar increase in oxygen-content values on decreasing the difference in the ionic-radii values between $Ln^{3+}$ and $Ba^{2+}$ in $LnBaCo_2O_{5+\delta}$ has been observed before, with a structural change from orthorhombic (Ln = Sm, Eu, Gd, and Tb) to tetragonal (Ln = Pr and Nd).[4-10] Figure 3 shows the relationship between the room-temperature oxygen content $(5+\delta)$ and the difference in ionic radii between $(Ba_{1-x}Sr_x)^{2+}$ and $Ln^{3+}$ $(r_A^{2+}\text{-}r_{Ln}^{3+})$ for the $Gd(Ba_{1-x}Sr_x)Co_2O_{5+\delta}$ and $LnBaCo_2O_{5+\delta}$ (Ln = La, Nd, Sm, Gd, and Y) samples synthesized in air; for a comparison, the ionic-radii values used in Fig. 3 are all for 12-coordination, and they are listed in Table III.[23-26] For smaller lanthanide ions like $Gd^{3+}$ and $Y^{3+}$, for which the12-coordinated radii are not available, the ionic radii for 12 cordination were obtained by extrapolating their 8-coordinated ionic-radii values. Both series of samples exhibit a linear relationship between oxygen nonstoichiometry and the ionic size difference $(r_A^{2+}\text{-}r_{Ln}^{3+})$. The larger the size difference between $(Ba_{1-x}Sr_x)^{2+}$ and $Ln^{3+}$, the greater the tendency of $(Ba_{1-x}Sr_x)^{2+}$ and $Ln^{3+}$ to order on the alternate planes along the $c$ axis and lower the oxygen content, as $Ln^{3+}$ tends to have less than 12 coordination. Thus, the trend in Fig. 3 may be useful to predict the oxygen content based on the size difference between the $A^{2+}$ and $Ln^{3+}$ ions in $ALnCo_2O_{5+\delta}$ perovskites.

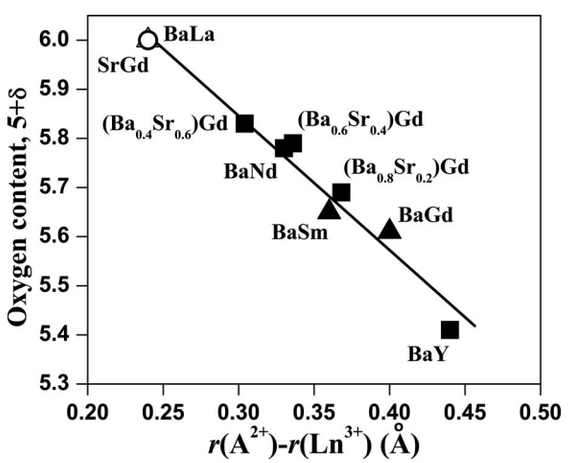


**Figure 3.** Variations of the room-temperature oxygen content $(5+\delta)$ values with the difference in ionic radii between $(Ba_{1-x}Sr_x)^{2+}$ and $Ln^{3+}$ $(r_A^{2+}\text{-}r_A^{3+})$ in the $Gd(Ba_{1-x}Sr_x)Co_2O_{5+\delta}$ and $LnBaCo_2O_{5+\delta}$ (Ln = La, Nd, Sm, Gd, and Y) samples synthesized in air. The different symbols refer to different crystal structures: ○: cubic (*Pm*-3*m*), ■: tetragonal (*P*4/*mmm*), ▲: orthorhombic (*Pmmm*), and △: orthorhombic (*Pnma*).

**Table III. Comparison of the ionic-radii values of the lanthanide and alkaline earth ions for 12 coordination.[26]**

| Ion | Ionic radius (Å) |
|---|---|
| $Ba^{2+}$ | 1.60 |
| $Sr^{2+}$ | 1.44 |
| $La^{3+}$ | 1.36 |
| $Nd^{3+}$ | 1.27 |
| $Sm^{3+}$ | 1.24 |
| $Gd^{3+}$ | 1.21[a] |
| $Y^{3+}$ | 1.17[a] |

[a] The values were obtained by extrapolating their 8-coordinated values.

Figure 4 shows the variations of the oxygen content and oxidation state of cobalt with temperature in air for the $GdBa_{1-x}Sr_xCo_2O_{5+\delta}$ $(0 \leq x \leq 1.0)$ samples. These curves were derived using the initial room-temperature oxygen-content values determined by iodometric titration and TGA data collected in air. The $GdBa_{1-x}Sr_xCo_2O_{5+\delta}$ samples lose oxygen on heating with a reduction of $Co^{4+}$ to $Co^{3+}$ as shown below using the Kroger–Vink notation[27]

$$2Co_{Co}^{\cdot} + O_O^X \leftrightarrow 2Co_{Co}^X + V_O^{\cdot\cdot} + 1/2O_2 \quad [1]$$

In the case of $0 \leq x \leq 0.4$ samples, the $Co^{3+}$ ions in $GdBa_{1-x}Sr_xCo_2O_{5+\delta}$ are further reduced to $Co^{2+}$ on heating to 900°C as shown below

$$2Co_{Co}^X + O_O^X \leftrightarrow 2Co_{Co}^I + V_O^{\cdot\cdot} + 1/2O_2 \quad [2]$$

All the samples lose 0.35–0.4 oxygen atoms per formula unit on heating to 900°C. However, at a given temperature, the oxidation state of cobalt increases with Sr content due to the higher initial, room-temperature oxygen-content values (Table I).

Figure 5 shows thermal-expansion curves of the $GdBa_{1-x}Sr_xCo_2O_{5+\delta}$ samples measured in air. The $GdBa_{1-x}Sr_xCo_2O_{5+\delta}$ samples show a linear expansion in the low-temperature region and an increase in slope at higher temperatures (>300°C). The increasing slope is due to the loss of oxygen from the lattice at high temperatures and the consequent reduction of smaller $Co^{4+}$ to larger $Co^{3+}$ or $Co^{2+}$ ions as revealed by the TGA data (Fig. 4). Thermal expansion curves were found to be reversible in the subsequent heating and cooling cycles. Thermal cycling was repeated three times in the temperature range of 80–900°C, and the average TEC values of the three cycles are given in Table I. Considering the oxygen loss from the lattice at $T > 300$°C (Fig. 4), the TEC values were calculated for two different temperature regions:

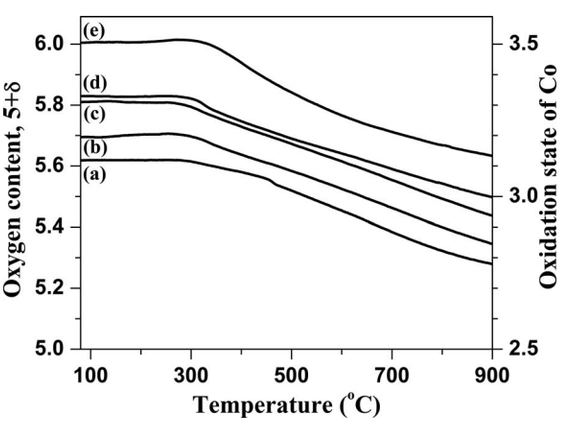


**Figure 4.** Variations of the oxygen content and the oxidation state of cobalt in the $GdBa_{1-x}Sr_xCo_2O_{5+\delta}$ with temperature in air: (a) $x = 0$, (b) $x = 0.2$, (c) $x = 0.4$, (d) $x = 0.6$, and (e) $x = 1.0$.

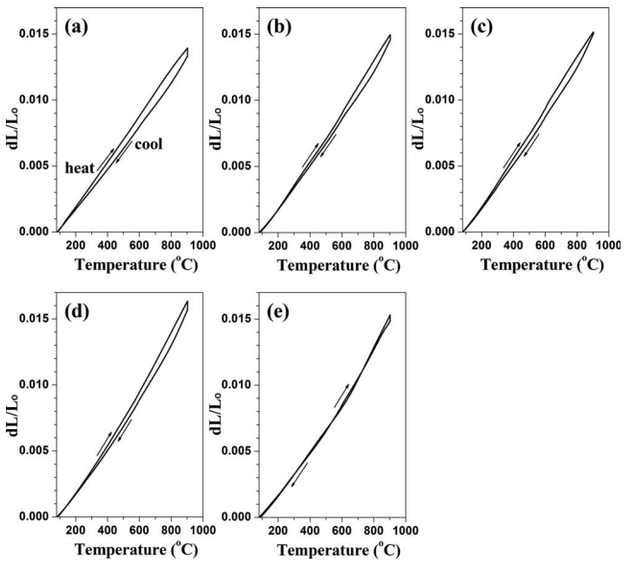


**Figure 5.** Thermal expansion ($dL/L_o$) curves of the $GdBa_{1-x}Sr_xCo_2O_{5+\delta}$ samples in the temperature range of 80–900°C in air: (a) $x = 0$, (b) $x = 0.2$, (c) $x = 0.4$, (d) $x = 0.6$, and (e) $x = 1.0$.

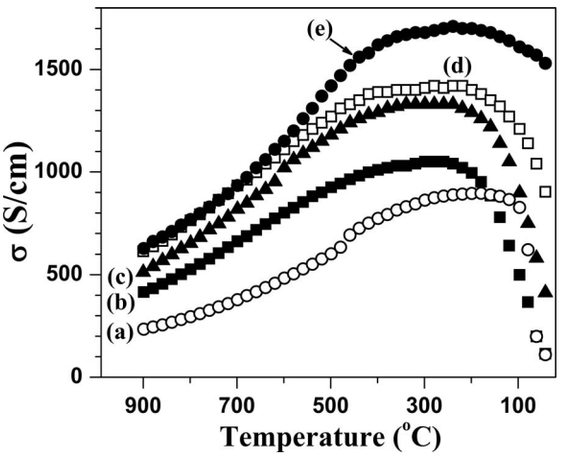


**Figure 6.** Temperature dependence of the electrical conductivity of the $GdBa_{1-x}Sr_xCo_2O_{5+\delta}$ samples in air: (a) $x = 0$, (b) $x = 0.2$, (c) $x = 0.4$, (d) $x = 0.6$, and (e) $x = 1.0$.

80–300 and 300–900°C. In the low-temperature region (80–300°C) where oxygen loss is negligible, TEC decreases with increasing Sr content, which could be due to the replacement of more-ionic Ba–O bonds with the less–ionic Sr–O bonds. In contrast, in the high–temperature region (300–900°C) where oxygen loss occurs, TEC increases with increasing Sr content, which can be understood by considering the spin-state transition associated with the $Co^{3+}$ ions. For example, the high TEC of the cobalt-containing perovskites (e.g., $LnCoO_3$) has been considered to be due to the low-spin $Co^{III}(t_{2g}^6e_g^0)$ to intermediate-spin $Co^{iii}(t_{2g}^5e_g^1)$ or high-spin $Co^{3+}(t_{2g}^4e_g^2)$ transitions.[2,28,29] Although the oxidation state of cobalt below 300°C is around 3.1+ for the $x = 0$ sample, the oxidation state begins to fall below 3+ for $T > 500$°C and reaches 2.77+ at 900°C as seen in Fig. 4, and $Co^{2+}$ remains in the high-spin state. The concentration of $Co^{3+}$ ions in the temperature range 300–900°C increases with increasing Sr content, and the $x = 0.4$ and 0.6 samples have the maximum amount of $Co^{3+}$ ions, which undergo spin-state transition. As a result, TEC increases on increasing the Sr content from 0 to 0.6 (Table I). However, the $x = 1.0$ sample has a lower concentration of $Co^{3+}$ ions than the $x = 0.6$ sample in the temperature range of 300–900°C, resulting in a decrease in TEC for the $x = 1.0$ sample. The $Co^{4+}$ ions are known to exist in the low-spin $Co^{IV}(t_{2g}^5e_g^0)$ state without undergoing spin-state transitions.

Figure 6 shows the variations of electrical conductivity with temperature for the $GdBa_{1-x}Sr_xCo_2O_{5+\delta}$ samples. All the $GdBa_{1-x}Sr_xCo_2O_{5+\delta}$ samples show a decrease in electrical conductivity with increasing temperature for $T > 300$°C due to an increasing concentration of oxygen vacancies. However, there is a sudden drop in conductivity at low temperatures ($T < 200$°C). The parent $GdBaCo_2O_{5+\delta}$ has been reported to have an M-I transition below 100°C (see Fig. 6a) due to an ordering of the low-spin $Co^{III}(t_{2g}^6e_g^0)$ and intermediate-spin $Co^{iii}(t_{2g}^5e_g^1)$.[1,4] Thus, the drop in conductivity below 200°C for the $0 \leqslant x \leqslant 1.0$ samples is due to M-I transition. However, the transition becomes less pronounced with increasing Sr content due to the increasing oxidation state of cobalt (Table I and Fig. 4) and the consequent decrease in oxide ion vacancy concentration and increase in the Co–O covalency and bandwidth.[30-32] For the same reason, at a given temperature, the electrical conductivity increases with increasing Sr content due to the increasing oxygen content. In addition, Sr substitution for $0.2 \leqslant x \leqslant 0.6$ relieves the compressive stress in the O–Co–O bonding due to a decreasing size of the cobalt ions (i.e., increasing $Co^{4+}$ content) and increases the O–Co–O bond angle toward the ideal value of 180°, as evidenced by the structural change from orthorhombic to tetragonal. The straightening of the O–Co–O bonds increases the overlap between the Co:3d and O:2p orbitals and consequently the electrical conductivity.[31-33] All the $GdBa_{1-x}Sr_xCo_2O_{5+\delta}$ samples show conductivity >300 S/cm up to 800°C, which is adequate for the samples to be employed as cathodes in SOFCs.

The chemical stability of the $GdBa_{1-x}Sr_xCo_2O_{5+\delta}$ cathodes in contact with the GDC and LSGM electrolyte was assessed by heating the mixed powders at 1100°C for 1 and 0.5 h, respectively. Figure 7 compares the XRD patterns of the $GdBa_{1-x}Sr_xCo_2O_{5+\delta}$ and GDC mixtures after heating at 1100°C for 1 h. Several new reflections corresponding to $BaCoO_{3-\delta}$ (JCPDS # 52-0429) can be noticed in Fig. 7a and b, indicating severe interfacial reaction of the $x = 0$ and 0.2 samples with GDC. However, further Sr substitution ($0.4 \leqslant x \leqslant 1.0$) greatly improves the chemical stability of the $GdBa_{1-x}Sr_xCo_2O_{5+\delta}$ samples with the GDC, showing no impurity reflections in Fig. 7c-e. Figure 8 compares the XRD patterns of the $GdBa_{1-x}Sr_xCo_2O_{5+\delta}$ and LSGM mixtures after heating at 1100°C

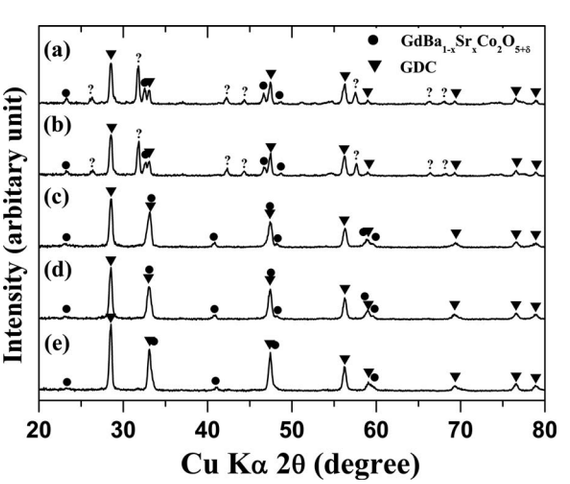


**Figure 7.** XRD patterns of the $GdBa_{1-x}Sr_xCo_2O_{5+\delta}$ and GDC mixtures after firing at 1100°C for 1 h in air: (a) $x = 0$, (b) $x = 0.2$, (c) $x = 0.4$, (d) $x = 0.6$, and (e) $x = 1.0$. Some of the reflections marked with ? belong to $BaCoO_{3-\delta}$.

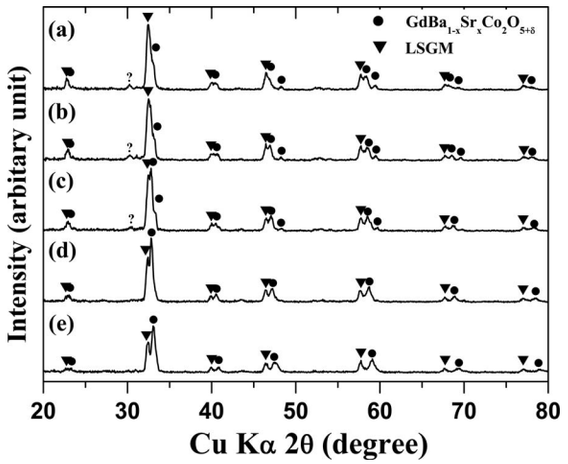


**Figure 8.** XRD patterns of the $GdBa_{1-x}Sr_xCo_2O_{5+\delta}$ and LSGM mixtures after firing at 1100°C for 0.5 h in air: (a) $x = 0$, (b) $x = 0.2$, (c) $x = 0.4$, (d) $x = 0.6$, and (e) $x = 1.0$. The reflections marked with ? belong to unknown phases.

for 0.5 h. While the $x = 0$–0.4 samples show a weak impurity reflection at $2\theta \approx 30°$ in Fig. 8a-c, the $x = 0.6$ and 1.0 samples show no impurity reflections in Fig. 8d and e. The results thus demonstrate that the substitution of Sr for Ba improves the chemical stability of the $GdBa_{1-x}Sr_xCo_2O_{5+\delta}$ samples in contact with the LSGM and GDC electrolytes at high temperatures.

The microstructures of the single cells were assessed by SEM. Figure 9 shows the cross sections of the $GdBa_{1-x}Sr_xCo_2O_{5+\delta}$ ($0 \leqslant x \leqslant 1.0$) cathode/composite electrode (cathode + LSGM)/LSGM electrolyte interfaces after the fuel cell performance test. Although the composite layer (cathode + LSGM) may not be necessary with the mixed conducting perovskite cathodes, it was introduced in the present study to provide good adhesion between the LSGM electrolyte and the $GdBa_{1-x}Sr_xCo_2O_{5+\delta}$ cathodes. While the bottom of the micrograph indicates a dense, well-sintered LSGM electrolyte, the upper portion shows the porous cathode/composite electrodes. The SEM images indicate good adhesion and continuous contact at the interfaces.

The performance of the $GdBa_{1-x}Sr_xCo_2O_{5+\delta}$ cathodes in SOFCs for the ORR was evaluated using LSGM as an electrolyte. Figure 10 shows the current–voltage curves and the corresponding power-density curves measured at 700, 750, and 800°C for the $GdBa_{1-x}Sr_xCo_2O_{5+\delta}$ ($0 \leqslant x \leqslant 1.0$) cathodes. The open-circuit voltages of the $GdBa_{1-x}Sr_xCo_2O_{5+\delta}$ cells were typically 1.10 V at 800°C, which is close to the theoretical value. There is a slight improvement in the fuel cell performance on substituting Ba par-

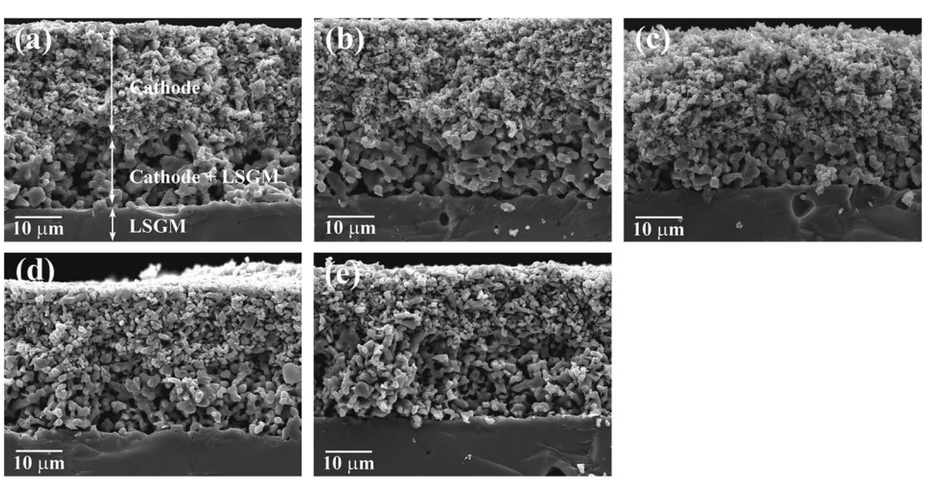


**Figure 9.** SEM micrographs showing the cross sections of the $GdBa_{1-x}Sr_xCo_2O_{5+\delta}$/$GdBa_{1-x}Sr_xCo_2O_{5+\delta}$–LSGM composite/LSGM portion of single-cell SOFC: (a) $x = 0$, (b) $x = 0.2$, (c) $x = 0.4$, (d) $x = 0.6$, and (e) $x = 1.0$.

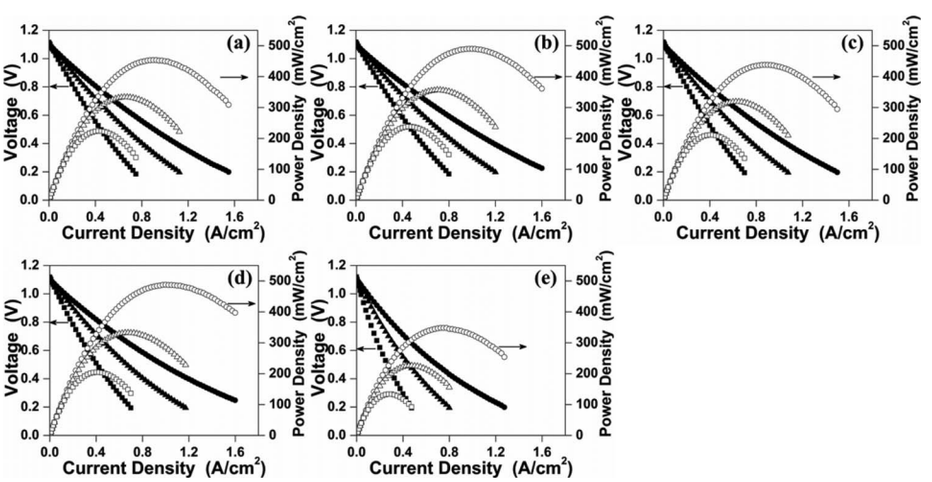


**Figure 10.** Electrochemical performance data of the $GdBa_{1-x}Sr_xCo_2O_{5+\delta}$/$GdBa_{1-x}Sr_xCo_2O_{5+\delta}$–LSGM/LSGM/LDC/Ni–GDC single cells at 700°C (square), 750°C (triangle), and 800°C (circle): (a) $x = 0$, (b) $x = 0.2$, (c) $x = 0.4$, (d) $x = 0.6$, and (e) $x = 1.0$.

tially with Sr ($x = 0.2$ and 0.6 samples) as seen in Fig. 10b and d. For example, the maximum power density ($P_{max}$) increased from 450 ($x = 0$) to 490 mW/cm$^2$ ($x = 0.2$ and 0.6). However, the $x = 0.4$ sample shows a slight decrease in $P_{max}$ to 440 mW/cm$^2$ compared to the $x = 0$ sample, and the $x = 1.0$ sample exhibits the lowest performance with a $P_{max} = 350$ mW/cm$^2$. Because all the samples have high enough electrical conductivity as seen in Fig. 6, the variations in fuel cell performance of the $0 \leqslant x \leqslant 0.6$ samples could possibly be related to the changes in the ionic conductivity and catalytic activity. Recent studies on the oxide ion diffusion and surface-exchange kinetics of the $LnBaCo_2O_{5+\delta}$ (Ln = Pr and Gd) samples have shown that the Ln = Pr sample with a tetragonal structure exhibits faster oxygen transport in the bulk and surface than the Ln = Gd sample with an orthorhombic structure.[12,13] Our previous study also showed that the Ln = Nd sample with a tetragonal structure in the $LnBaCo_2O_{5+\delta}$ system exhibits higher catalytic activity for the ORR than the Ln = Sm and Gd samples with an orthorhombic structure.[10] Therefore, the enhanced catalytic activity of the $x = 0.2$ and 0.6 samples (tetragonal) could be related to the faster oxygen transport compared to that in the $x = 0$ and 1.0 samples (orthorhombic). Our future studies will focus on the oxide ion transport mechanisms in the $GdBa_{1-x}Sr_xCo_2O_{5+\delta}$ system.

## Conclusions

The effect of Sr substitution for Ba in the double perovskite $GdBa_{1-x}Sr_xCo_2O_{5+\delta}$ has been investigated. The $GdBa_{1-x}Sr_xCo_2O_{5+\delta}$ system exhibits a structural change from orthorhombic ($x = 0$) to tetragonal ($x = 0.2$–0.6) to orthorhombic ($x = 1.0$) with changes in space groups and an increase in oxygen content ($5 + \delta$) with increasing Sr content. While the TEC decreases with increasing Sr content in the low-temperature region (80–300°C), it increases with Sr content in the high-temperature region (300–900°C). The $GdBa_{1-x}Sr_xCo_2O_{5+\delta}$ samples exhibit an M-I transition around 200°C and the transition becomes less pronounced with increasing Sr content. At a given temperature, the electrical conductivity increases with increasing Sr content due to increasing oxygen content. While the parent $GdBaCo_2O_{5+\delta}$ sample suffers from interfacial reaction with LSGM and GDC electrolytes at 1100°C, Sr substitution for Ba greatly improves the chemical stability of $GdBa_{1-x}Sr_xCo_2O_{5+\delta}$. The $x = 0.2$ and 0.6 samples exhibit higher power density in SOFC than the $x = 0$ and 1.0 samples, partly due to faster oxygen transport within the tetragonal structure compared to that in the orthorhombic structure ($x = 0$ and 1.0).

## Acknowledgments

Financial support by the Welch Foundation grant F-1254 and ANPCyT through PICT 2006-00829 in Argentina is gratefully acknowledged.

*University of Texas at Austin assisted in meeting the publication costs of this article.*

## References

1. C. Martin, A. Maignan, D. Pelloquin, N. Nguyen, and B. Raveau, *Appl. Phys. Lett.*, **71**, 1421 (1997).
2. I. O. Troyanchuk, N. V. Kasper, and D. D. Khalyavin, *Phys. Rev. B*, **58**, 2418 (1998).
3. T. Vogt, P. M. Woodward, P. Karen, B. A. Hunter, P. Henning, and A. R. Moodenbaugh, *Phys. Rev. Lett.*, **84**, 2969 (2000).
4. Y. Moritomo, M. Takeo, X. J. Liu, T. Akimoto, and A. Nakamura, *Phys. Rev. B*, **58**, R13 334 (1998).
5. A. Maignan, C. Martin, D. Pelloquin, N. Nguyen, and B. Raveau, *J. Solid State Chem.*, **142**, 247 (1999).
6. A. Chang, S. J. Skinner, and J. A. Kilner, *Solid State Ionics*, **177**, 2009 (2006).
7. D. Akahoshi and Y. Ueda, J. Solid *J. Solid State Chem.*, **156**, 355 (2001).
8. J. C. Burley, J. F. Mitchell, S. Short, D. Miller, and Y. Tang, *J. Solid State Chem.*, **170**, 339 (2003).
9. C. Frontera, A. Caneiro, A. E. Carrillo, J. Oró-Solé, and J. L. García-Muñoz, *Chem. Mater.*, **17**, 5439 (2005).
10. J.-H. Kim and A. Manthiram, *J. Electrochem. Soc.*, **155**, B385 (2008).
11. A. A. Taskin, A. N. Lavro, and Y. Ando, *Appl. Phys. Lett.*, **86**, 091910 (2005).
12. G. Kim, S. Wang, A. J. Jacobson, L. Reimus, P. Brodersen, and C. A. Mims, *J. Mater. Chem.*, **17**, 2500 (2007).
13. A. Tarankon, S. J. Skinner, R. J. Chater, F. H. Ramírez, and J. A. Kilner, *J. Mater. Chem.*, **17**, 3175 (2007).
14. L. A. Chick, L. R. Pedersen, G. D. Maupin, J. L. Bates, L. E. Thomas, and G. J. Exarhos, *Mater. Lett.*, **10**, 6 (1990).
15. H. Taguchi, D. Mastuda, M. Nagao, K. Tanihata, and Y. Miyamoto, *J. Am. Ceram. Soc.*, **75**, 201 (1992).
16. J. Rodriguez-Carjaval, *Physica B*, **192**, 55 (1993).
17. A. Manthiram, J. S. Swinnea, Z. T. Sui, H. Steinfink, and J. B. Goodenough, *J. Am. Chem. Soc.*, **109**, 6667 (1987).
18. L. J. Van der Pauw, *Philips Res. Rep.*, **13**, 1 (1958).
19. I. Reiss, *J. Appl. Phys.*, **71**, 4079 (1992).
20. J. Wan, J. H. Zhu, and J. B. Goodenough, *Solid State Ionics*, **177**, 1211 (2006).
21. P. V. Vanitha, A. Arulraj, P. N. Santhosh, and C. N. R. Rao, *Chem. Mater.*, **12**, 1666 (2000).
22. X. G. Luo, H. Li, X. H. Chen, Y. M. Xiong, G. Wu, G. Y. Wang, C. H. Wang, W. J. Miao, and X. Li, *Chem. Mater.*, **18**, 1029 (2006).
23. R. D. Shannon, *Acta Crystallogr.*, **32**, 751 (1976).
24. J. Nakamura, M. Karppinen, P. Karen, J. Lindén, and H. Yamauchi, *Phys. Rev. B*, **70**, 144104 (2004).
25. P. Karen, *J. Solid State Chem.*, **177**, 281 (2004).
26. *Lange's Handbook of Chemistry*, 5th ed., J. A. Dean, Editor, pp. 4.30–4.34, McGraw-Hill Inc., New York (1999).
27. F. A. Kroger and H. J. Vink, in *Solid State Physics*, F. Seitz and D. Turnbull, Editors, Vol. 3, p. 307, Academic Press, New York (1956).
28. M. A. Señarís-Rodríguez and J. B. Goodenough, *J. Solid State Chem.*, **118**, 323 (1995).
29. K. Huang, H. Y. Lee, and J. B. Goodenough, *J. Electrochem. Soc.*, **145**, 3220 (1998).
30. H. Takahashi, F. Munakata, and M. Yamanaka, *Phys. Rev. B*, **57**, 15211 (1998).
31. K. T. Lee and A. Manthiram, *J. Electrochem. Soc.*, **153**, A794 (2006).
32. K. T. Lee and A. Manthiram, *J. Electrochem. Soc.*, **152**, A197 (2005).
33. G. C. Kostogloudis, N. Vasilakos, and C. Ftikos, *Solid State Ionics*, **106**, 207 (1998).